DOI: 10.2478/fas-2023-0006
FATIGUE OF AIRCRAFT STRUCTURES
Volume 2023: Issue 15, pp. 90–114

DEVELOPMENT OF DIFFRACTION RESEARCH METHODOLOGIES FOR MEDILOY S-CO ALLOY SPECIMENTS MADE USING LPBF ADDITIVE MANUFACTURING

Elżbieta Gadalińska*, Maciej Malicki, Anna Trykowska, Grzegorz Moneta
Łukasiewicz Research Network – Institute of Aviation
Al. Krakowska 110/114, 02-256 Warsaw, Poland.

elzbieta.gadalinska@ilot.lukasiewicz.gov.pl

Abstract

This study focuses on the application and improvement of diffraction measurement methodologies for the optimization of manufacturing parameters of CoCr alloy components made by additive manufacturing (AM) – particularly for Mediloy S-Co alloy specimens made using Laser Powder Bed Fusion (LPBF) additive manufacturing. We measured the phase composition of specimens obtained in AM processes, the measurement of residual stresses resulting from the manufacture of these printed parts, as well as the effectiveness of stress relaxation through the use of heat treatments dedicated to this type of material. Findings reveal several insights into how printing strategies affect the porosity and residual stresses in additive manufacturing. Specimens with higher porosity, particularly those created using specific strategies that resulted in lower energy densities, exhibited lower residual stresses. Notably, printing direction and energy density were found to significantly affect the mechanical stresses within the specimens, with directional choices playing a critical role in the final properties of the parts. Additionally, our findings underscore the complex relationship between various printing parameters and the development of mechanical stresses, highlighting the impact of adjustments in printing strategy on the properties of printed components.

Keywords: diffraction, phase analysis, stress, additive manufacturing, selective laser melting (SLM), Mediloy S-Co, Laser Powder Bed Fusion (LPBF).
Article Category: research article, experimental

1. INTRODUCTION

Although the idea of incremental component manufacturing techniques is more than 40 years old, techniques of this type have yet to be widely implemented in mass production, still being hindered by challenges that make it difficult to obtain parts with acceptable strength properties. 3D printing processes make it possible to obtain parts with complex shapes or gradient-varying properties (known as functionally graded materials, FGM – see Bhavar et al., 2017), which in the long run can improve products across various industries; however, when it comes to metal 3D printing, the most problematic issues are significant surface roughness, the presence of pores inside the printed parts and the presence of surface tensile stresses. Certain established procedures already exist by which it is possible to eliminate residual stresses with undesirable tensile values (appropriate post-printing thermal treatment, use of a multiple laser pass procedure, heating of the print platform before the printing process). Processes are also being developed to significantly change the stresses, i.e. to introduce compressive stresses in place of tensile stresses using methods such as grinding, drag finishing, shot-peening or laser shock peening (LSP) (Pathak et al., 2023; Behjat et al., 2023). Hot isostatic pressing (HIP), in turn, makes it possible to get rid of excess, unwanted porosity.

This paper examines the properties of cobalt–chromium (CoCr) alloy printed parts obtained using the selective laser melting (SLM) method. Castings made of this alloy are usually characterized by grains of considerable size, a rather heterogeneous structure and defects within the material, resulting from the solidification process. As a result, the resulting parts suffer from inadequate mechanical properties and uneven quality. The advantage of incremental manufacturing methods lies in the ability to optimize the printing parameters in such a way as to avoid such problems. They key parameters in the printing process primarily include scanning speed, laser power, and standing strategies. In the case of alloys from the CoCr family, the optimization of these parameters proves to be particularly important because it greatly affects the microstructure and properties of the final product.

In general, cobalt–chromium alloys contain two main phases: γ-fcc (face centered cubic) and ε-hcp (hexagonal close packed) phases. The γ-fcc phase is thermodynamically stable at high temperatures (above 900°C), while the ε-hcp phase is stable at room temperature. Under certain conditions, the two phases can undergo a mutual transformation. The mechanical properties of these alloys are significantly influenced by the relative amount of γ-fcc and ε-hcp phases, as well as their grain sizes. For example, the volume fraction of the ε-hcp phase strongly influences work hardening and yield strength, but has little effect on tensile strength. On the other hand, an increase in the fraction of the ε-hcp phase results in an increase in hardness and wear resistance, but has a degrading effect on the ductility of alloys (Wei, Koizumi, Chiba, et al., 2018).

The influence of heat treatment on the microstructure and mechanical properties of Co-Cr-Mo alloy obtained by conventional methods was investigated by Lee et al. (2005). Four pre-heat treatments were performed at 1170, 1200, 1230 and 1260°C for three different time conditions: 2, 6, 15h. After every heat treatment the specimens were water-cooled. Tensile tests and X-ray diffraction analyses were used to examine the

microstructure and mechanical properties. The volume fraction of the γ phase was found to increase with higher heat treatment temperature. These findings indicate that the suppression of γ → ε transformation takes place with increasing heat treatment temperature. Lee et al. (2005) also noted a slight decrease in tensile strength and an increase in ductility as both the temperature and duration of heat treatment were raised. It was observed that heat treating the alloy at 1260°C for more than 6 hours completely dissolved the σ phase.

Conversely, the study by Gaytan et al. (2010) focused on as-fabricated and fabricated and annealed femoral prototypes and reticulated mesh components, all produced with additive manufacturing, using electron beam melting (EBM). The CoCr alloy selected for this study was Co-26Cr-6Mo-0.2C. Optical metallography, scanning electron microscopy, transmission electron microscopy, energy-dispersive X-ray spectrometry, X-ray diffraction, tensile and hardness tests were involved. In this study, the fact of transformation from the hexagonal ε phase to the face-centred γ phase was confirmed also for additively manufactured elements. It was pointed out that this transformation occurs at a temperature of 430°C; with the addition of Cr this temperature increases to 970°C. The γ → ε transformation can also occur as an effect of plastic deformation or quenching from the temperature range of the stable γ phase. Quenching from the melt state results in the formation of a primarily γ phase while rapid solidification leads to the formation of a mixed phase. The EBM fabrication of Co-26Cr-6Mo-0.2C alloy powder, in the initial state characterized by a hexagonal structure (hcp) of solid elements, results in a matrix with a fcc structure (CoCr with a CrMn component), with $Cr_{23}C_6$ fcc orthogonal carbide arrays when viewed perpendicular to the build direction and carbide columns connected to these arrays when viewed in a plane parallel to the build direction. These findings pave the way for future development of a set of EBM printing parameters to achieve controlled microstructural architectures. Moreover, the mechanical properties slightly increased with respect to wrought or cast Co-26Cr-0.6Mo alloys.

The study by Sun et al. (2014) examined the impact of EBM printing direction on the microstructural and high-temperature strength properties of the CoCrMo alloy. The occurrence of crystallographic texture was observed with printing tilt from the axis of the samples by 0°, 45°,55° and 90°. The preferred crystalline orientations of the γ phase in specimens produced by the EBM method with angles of 0°,45°,55° and 90° were close to [0 0 1], [1 1 0], [1 1 1] and [1 0 0], respectively. The regular occurrence of carbide precipitates at 3 μm intervals along the building direction was observed. Notably, transformation to the hcp phase after heat treatment at 800° for 24 h was also detected. Although no significant texture was observed after aging, lamellar nitride colonies appeared. Furthermore, the study found that printing in the 55° direction relative to the specimen axis provided the highest ultimate tensile strength (806 MPa at 700 degrees). It was concluded that determining the optimal heat treatment conditions for homogenizing the microstructure over the entire height of EBM-built objects should consider the thermal history in the post-melting period of the EBM process, especially when the solid-solid transition is slow.

In the study by Barucca et al. (2015), a Co-Cr-Mo alloy produced by direct metal laser sintering (DMLS) underwent hardness tests and structural analysis. Echoing

previous findings Xin et al. (2013), Mantrala et al. (2014), this study showed that the hardness value of this alloy is significantly higher than commonly obtained for the same cast or forged alloys. Seeking to explain this using X-ray diffraction (XRD), electron microscopy (SEM and TEM) and energy dispersive microanalysis (EDX), the study revealed a homogeneous microstructure consisting of an intricate network of thin ε (hcp)-lamellae distributed within the γ-phase (fcc). The authors conclude that the ε-phase lamellae that appeared on the {111} γ planes limit the dislocations movement inside the γ-phase (fcc), causing the measured increase in hardness.

The study presented in Qian et al. (2015), in turn, investigated the microstructure of CoCrMo specimens prepared with selective laser melting. The goal was to understand the influence of the structural characteristics of the alloy at different scales on the mechanical properties of the printed elements. The investigation found that, despite the presence of defects, the yield strength and ultimate tensile strength (UTS) were 870 and 430 MPa and 1300 MPa and 1160 MPa, respectively, for two types of specimens (called: 'core' and 'skin'), which are higher than for the cast dental alloy. Two different sets of processing parameters developed for the internal part ('core') and surface ('skin') structures of dental protheses were tested. For 'core' specimens the applied laser power was 190 W, scanning speed 535 mm/s, hatched line distance was 0.14 mm and layer thickness was 40 μm, while for 'skin' specimens these parameters were respectively: 190W, 800 mm/s, 0.1 mm and 20 μm. The microstructures were characterized by SEM, EBSD and XRD analyses. Elemental distributions were assessed by EDS line profile analysis under TEM. Mechanical properties of the samples were measured. Through testing, the formation of grains consisting of columnar sub-grains with Mo enrichment at the sub-grain boundaries was observed. Clusters of columnar grains grew coherently along one common crystallographic direction to form much larger monocrystalline grains that intersected in different directions to form an overall dendritic microstructure. Occasionally, three types of microstructural defects were observed: small voids (<10 μm), small cracks at grain boundaries (<10 μm) and cracks at weld line boundaries (>10 μm). Using X-ray diffraction (XRD) analysis at room temperature the authors showed that the surface of the specimens consisted of the metastable, high-temperature cubic γ (fcc) phase. This seemed consistent as the outer surfaces are rapidly cooled. After grinding and polishing of the surface, additional weak peaks of the low-temperature hexagonal ε phase was detected. The partial phase transformation from γ to ε phase might occur in the bulk interior due to slower cooling. An additional annealing of the specimen at 950°C for 6 min yielded a significant increase in the γ phase at the expense of ε phase; proving the solid-state transformation of the fcc structure at medium temperature.

Lu et al. (2015) focused on the microstructure, hardness, mechanical properties, electrochemical behavior and metal release of CoCrW alloy specimens (without nickel), printed with two types of printing strategy: line-scan and island-scan. XRD revealed that γ-phase and ε-phase coexisted in the as-SLM CoCrW alloys. Optical and scanning electron microscopy observations showed that the microstructure of the CoCrW alloys appeared as a square pattern with fine dendrite cells at the boundaries. Tensile testing suggested that the difference in mechanical properties of the line-formed and island-formed samples is very small.

The effects of heat treatment on components obtained using SLM incremental methods on microstructure, mechanical properties and metal release were investigated in Lu et al. (2016) using X-ray diffraction microscopy, tensile test and ICP-AES. XRD indicated that the alloy underwent a transformation from γ-fcc to ε-hcp phase during thermal processing. The ε-hcp phase almost dominated the alloy during processing at 1200°C after water quenching. Heat treatment at 1150°C with furnace cooling contributed to the formation of larger precipitates in the grain boundary regions, while the size and number of precipitates decreased after heating above 1100°C with water quenching. The diamond-like structure was invisible at higher solution temperatures above 1150°C after water quenching. The authors showed that, compared with furnace cooling, the water-hardened alloy exhibited excellent mechanical properties and a low amount of metal release. The mechanical properties of the alloy reached an optimum combination for the alloy heated in 1200°C: UTS = 1113.6 MPa, 0.2%YS = 639.5 MPa, and E% = 20.1%, while showing a lower total amount of metal release.

The study by Mengucci et al. (2016) looked at the effect of post-production treatments (shot peening, stress relieving, firing cycle) on the mechanical and microstructural properties of Co-Cr-Mo-W alloy prints obtained using Direct Metal Laser Sintering (DMLS). Experimental results showed the existence of a complex network of ε-Co lamellae in the γ-Co matrix responsible for the high UTS and hardness values in the sintered state. Heat treatment increased the volume proportion of ε-Co martensite, but slightly changed the average size of the lamellar structure. One of the main conclusions of the study is that heat treatment is able to induce a significant increase in UTS and hardness and a strong reduction in ductility.

Further confirmation of the existence of two phases (γ-fcc and ε-hcp) in the material of Co-Cr-Mo alloy parts using incremental methods can be found in Takashima et al. (2016). The authors concluded that their specimens positioned in the central part of the matrix consisted more of the γ-fcc phase and less of the ε-hcp phase than those in the matrix's outer part. The likely reason for this is that, although each specimen was produced under the same conditions, the specimens in the center were exposed to a higher temperature than the specimens in the outer part, and there was less heat dissipation as the neighboring specimens were also heated by the electron beam. This difference in thermal history should be taken into account when fabricating multiple objects simultaneously. The authors underline that the ε phase formed by the transformation from the γ phase gives rise to great changes in the mechanical properties, such as increased wear resistance together with a decrease in the ductility; therefore, it is important to control the phase distribution in additive-manufactured alloys.

Other sources (e.g. Wang et al., 2018), address the problem of microstructural changes and corrosion resistance after different treatments (e.g. laser polishing), applying modified printing parameters (e.g. laser power) or object distances. These results of this work indicate that laser polishing can improve the microstructure, surface structure and corrosion resistance of additively manufactured CoCr alloy by effectively controlling the hcp structures and the oxides formed. The experimental results indicated that the laser-polished samples have higher corrosion resistance and are about 30% better than some thermomechanically treated samples reported in previous studies. Furthermore, oxides on the outer layer and structures in the inner layer play an important

role in the corrosion resistance of laser-polished samples, and the most important parameters of the laser polishing process are laser power and object distance. This paper concludes that the difficulty of oxide growth is influenced by the directions of the ε phase, and the transformation of the crystalline phase from the γ phase to the ε phase is accompanied by vacancies and planar defects.

Different and temperature dependent crystallographic phases were also revealed by Wei, Koizumi, Chiba, et al. (2018) for Co-Cr-Mo alloy fabricated by electron beam melting. The authors investigated the phase composition of the printed element and found that the constituent phases of the top side (built later) differ from those of the bottom side (built earlier) of the rod. The upper side consists mainly of the γ-fcc phase, while the lower side consists of the ε-hcp phase. Both phases coexist in the middle part of the bar. The average grain size in the area of the element where the γ-fcc phase dominates is approx. 3 times lower than in the area of ε-hcp phase dominance. The local strain density is much higher in the later-printed part of the element and decreases with increasing distance from this part. A large number of precipitates were observed, which consisted of the main $M_{23}X_6$ phase and minor, η- and π-, phases, with surface proportions ranging from 5.3% (top) to 8.7% (bottom). The hardness of the samples, as well as the surface fraction of the precipitates formed in them, increases progressively from top to bottom of the bar.

The microstructure, phase composition, strength and corrosion properties of the Co-Cr-Mo-W alloy produced by the SLM process, in turn, were investigated in the study by Wei, Zhou, et al. (2018). The presence of a diverse microstructure was demonstrated, which is homogeneous, supersaturated and composed of extremely fine columnar crystals. Higher strength properties were demonstrated compared to cast components. The high strength is attributed to their fine-grained and supersaturated matrix causing consolidation at the grain boundary and strengthening in the supersaturated state. The lower HCP phase content and the absence of intermetallic compounds or eutectics contributed to the high ductility.

In the study by Monroy, Delgado, and Ciurana (2013), image analysis showed the existence of randomly distributed pores with smooth walls resulting from gas entrapment during the SLM incremental manufacturing process. The authors demonstrated the possibility of obtaining printed CoCrMo alloy dense printed parts, i.e. with the lowest porosity of 0.9%. The lowest porosity was obtained with the thickest layer. This had to do with a better packing of the powder particles, and thus a better thermal conductivity between the particles. The average pore size was independent of layer thickness or laser power, with a strong increase when scanning speed was reduced. The authors suggest this increase in pore size, corroborated by other studies, is due to the prolonged exposure of the material to high temperatures. The most important conclusion of the paper is its identification of the optimum printing process parameters for which the lowest porosity was obtained: a scanning speed of 50 mm/s and the highest possible layer thickness, here: 50 μm. Conversely, the pores with the smallest size were obtained at a scanning speed of 83.3 mm/s and a layer thickness of 500 μm.

Seeking understand the mechanism of defect formation, accurate three-dimensional images of defects inside SLM, Zhou et al. (2015) obtained fabricated Co-Cr-Mo samples by synchrotron radiation micro-CT imaging. The porosities remaining in

Co-Cr-Mo alloy parts prepared by selective laser melting were presented as a function of laser processing parameters. Accidental monolayer defects arose as gaps between adjacent laser melt paths or discontinuities in the melt paths, due to inherent fluid instability under the influence of various disturbances. The first monolayer defect formed often generates a multilayer defect involving 2-3 consecutive powder layers. By stabilizing the melt pool flow and reducing the surface roughness by adjusting the machining parameters, it is possible to reduce the concentration of defects.

The paper by Xin et al. (2013) investigates the corrosion features as well as the surface properties of a commercially available Co-Cr alloy (Co61.5, Cr26.0, W5.0, Mo6.0, Si, Fe) produced using the SLM method and compares the results of such components with those made using traditional casting methods. Hardness tests, microstructure observations, as well as surface analysis by XPS spectroscopy and an electrochemical corrosion test were carried out. The results showed that the microstructure of the printed samples was more homogeneous and their hardness was higher, averaging 458Hv compared to the cast samples, which had a hardness of 384Hv. There were no significant differences between the surface properties and corrosion properties of the printed and cast samples.

The microstructural properties, wear susceptibility and corrosion properties of laser engineered net shaped (LENS) components have been investigated and presented in Mantrala et al. (2014). The authors of this paper investigated the properties of deposits produced using different values of the manufacturing process parameters. They found that the deposits produced were characterized by a homogeneous microstructure. The coatings produced using high laser power (350 W), low powder feed rate (5 g/min) and high scanning speed (20 mm/s) were characterised by the highest hardness (446Hv) and wear resistance (1.80 mm^3/Nm). In contrast, corrosion resistance was observed at a high level for deposits produced using low laser power (200 W), low powder feed rate (5 g/min) and low scanning speed (10 mm/s). Electrochemical and metal release experiments performed in study Lu et al. (2015) indicate that the island-formed specimens made of CoCrW Ni-free alloys show slightly better corrosion resistance than the line-formed ones in PBS and Hanks solutions.

The mechanical properties and fatigue strength of SLM-produced Co-Cr alloy specimens were investigated by Kajima et al. (2016). The specimens were printed in three ways: with the print direction in line with the specimen axis, perpendicular to the specimen axis, and inclined at 45° to the specimen axis. The results were compared with the results for cast specimens. All groups of SLM alloys showed significantly higher 0.2% offset yield strength and tensile strength than the cast samples, which was probably due to the fine-grained microstructure of the SLM print-outs obtained by their rapid solidification. In contrast, SLM-prepared specimens showed significant anisotropy in fatigue strength. The fatigue strength of the specimen for which the print direction was perpendicular to the specimen axis was significantly higher than that of the cast specimens, while it was significantly lower for the other two specimen types. This phenomenon can be caused by many factors such as surface roughness, crystal orientation, residual stresses and melt pool boundaries.

The study by Wei, Koizumi, Takashima et al. (2018) investigated the effect of heat treatment and thus phase composition and microstructure induced fatigue properties

of Co-Cr-Mo alloy produced by EBM. It was observed that the strengths in stress-controlled fatigue were enhanced by converting the initial dual γ + ε phase into a dominant ε phase, and were then significantly improved by inversely converting the ε phase into a γ phase with refined grains. The improvement was achieved by manipulating the fatigue deformation behavior and refining the grain structures.

The primary aim of the present study, therefore, is to investigate the influence of additive manufacturing parameters on the microstructural characteristics and residual stress profiles of Mediloy S-Co alloy specimens produced through LPBF technology. Specifically, this study seeks to elucidate the relationship between printing strategies, porosity levels, and their subsequent impact on the mechanical integrity and stress distribution within printed parts. By analyzing these relationships, we seek to contribute to optimizing printing parameters, thereby enhancing the quality, performance, and application potential of CoCr alloy components in various industrial domains.

2. MATERIAL, SPECIMENS AND HEAT TREATMENTS

2.1. Material

A material with the commercial name Mediloy S-Co, which is an alloy of cobalt with chromium, was selected for the study. The percentage of alloying elements of this material is included in the Table 1.

Table 1. Chemical composition of Mediloy S-Co alloy.

Co	Cr	Mo	W	Si
63.9 %	24.7 %	5 %	5.4 %	<1 %

This alloy is mainly used in dentistry (bridges, crowns, abutments) and is characterized by exceptional mechanical properties such as toughness, corrosion resistance and geometrical stability. In addition, it is distinguished by excellent bio-compatibility, very good machinability and weldability. The density of this alloy is 8.6 kg/dm^3.

2.2. Specimens

The series of diffraction measurements carried out on the specimens presented in this study are part of a project aiming to develop SLM printing parameters for CoCr alloy components. A total of 15 specimens with cylindrical geometries dedicated to high-cycle fatigue testing were fabricated on SISMA MYSINT100 LPBF machine to meet the project's objectives. In the present study, specimens numbered 1 to 5 are those for which the printing direction was the same as that of the specimen axis; specimens numbered 6 to 10 are those for which the printing direction was inclined by 45º with respect to the specimen axis, while specimens 11 to 15 are those printed in a direction perpendicular to their axis. Each of the 5 specimens printed in one of these three orientations was produced using the parameters proposed in Table 2. These sets were developed based on previous experience with SLM printing of CoCr alloy components and the results of numerical simulations of the additive manufacturing

process. The choice of process parameters was dictated by the desire to obtain a wide range of intentional material defects. The printed specimens are presented in Fig. 1. A summary of the print parameters and porosity of the samples thus obtained is presented in Table 2. For information on the optimal set of parameters (No. 1), no details are given due to intellectual property protection. Instead, information is given on the energy density calculated from the following formula (Gong et al., 2014):

$$ED_{VH} = \frac{P}{VHt} \tag{1}$$

where:
P – laser power [W], V – scanning speed [mm/s], H – hatch spacing [mm], t – layer thickness [mm].

Table 2. Printing parameters, energy densities and porosities for all parameter sets.

Printing parameters set no.	Laser power [W]	Scanning speed [mm/s]	Single layer thickness [mm]	Hatch spacing [mm]	Energy density [J/mm^3]	Porosity [%]
1	optimized parameter set				119.8	0.05%
2	95	1000	0.35	0.09	30.2	8.06%
3	120	1200	0.03	0.075	44.4	1.60%
4	70	1200	0.02	0.105	27.8	16.81%
5	145	800	0.02	0.06	151.0	Ref.

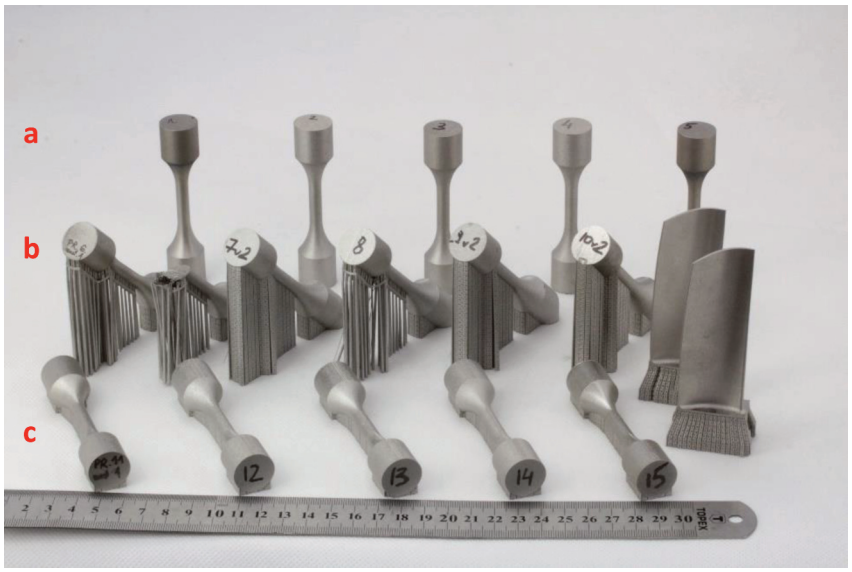

Fig. 1. The printed specimens of all 3 directions and all 5 printing sets.
The specimens printed in the direction parallel to their axis (row a), inclined 45º to their axis (row b), and perpendicular to their axis (row c).

2.3. Heat treatments

The heat treatment procedure was carried out in a Nabertherm LT 9/11/C450 furnace. The specimens were arranged starting from the rear wall of the furnace so as to eliminate the possible undesirable effect of the temperature drop at the furnace door. In a separate heat treatment cycle, the temperature waveforms over time were checked both in and next to the 10×10×10 mm^3 specimen material. For this experiment, K-type thermocouples and a Lutron TM-947SD temperature recorder were used. The analysis showed a great convergence in the rate of temperature rise between the set program and the actual values. The maximum temperature achieved exceeds that given by about 20°C. During heat treatment, differences were observed between the temperature of the furnace and the temperature of the specimen. After exceeding 100°C, the temperature of the specimen began to rise faster than the furnace temperature, and the maximum temperature difference was reached at about 600°C and was about 20°C. With further heating, the temperature difference began to decrease. The heat-treated specimens are covered by a black-green layer as a result of annealing in an air atmosphere. The resulting oxide and nitride layer on the surface of materials is usually an undesirable effect and can be removed by subjecting the parts to cavity treatment, for example. Oxidation can be reduced using a protective atmosphere during processing or using vacuum processing.

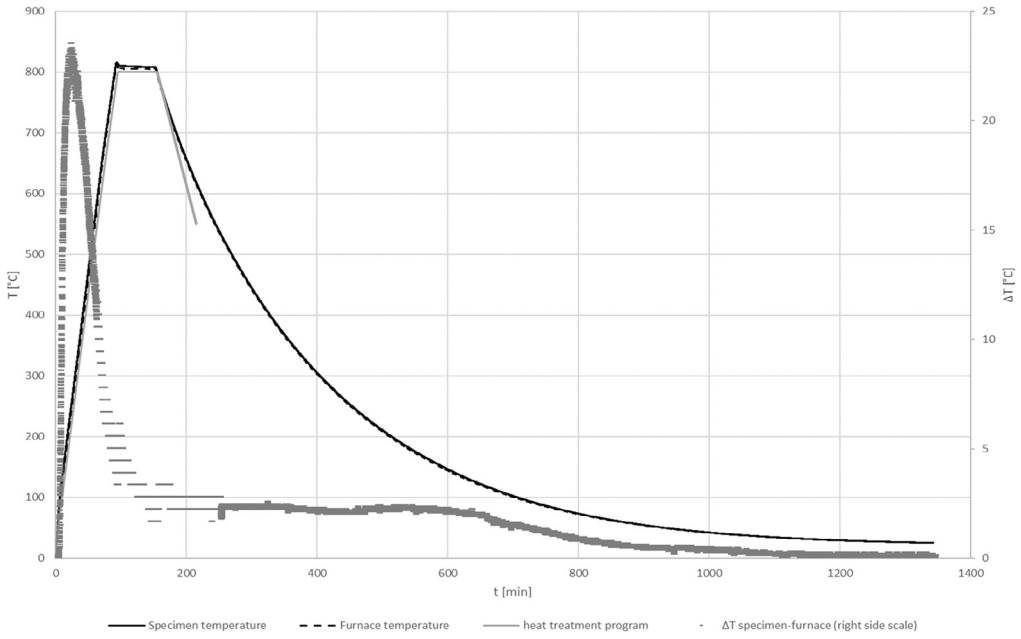

Fig. 2. Temperature change during heat treatment.

3. EXPERIMENTAL RESULTS

3.1. Microstructural observations

3.1.1. Material in as-built state

The microstructure was observed both before and after heat treatment. In the case of non-heat-treated specimens, these observations were performed for specimens produced using parameter set no. 1 (see Table 2), with which a 10×10×10 mm^3 cubic specimen was printed. The main goal in this case was to select the most suitable etchant. Various etching methods were used, with a large share of them coming from ASTM Standard E407 (Kundra, 2023):

- swab with cotton using H_2O_2 solution in hydrochloric acid (etchant no. 22 according to Kundra (2023): 100ml HCl + 0.5ml H_2O_2 (30%)).
- electrolytic etching using H_2O_2 solution in hydrochloric acid (ref. no. 22 according to Kundra (2023): 100ml HCl + 0.5ml H_2O_2 (30 %)) at 4V.
- immersion in Kalling's etchant 1 and 2.
- electrolytic etching using 10% aqueous solution of oxalic acid at 6V.
- swab with 38% aqueous solution of hydrochloric acid.
- electrolytic etching using HNO_3 + 40ml H_2O solution at 1V (ref. no. 219 according to Kundra, 2023).
- immersion in Berach's etchant III with the addition of sodium pyrosulfate (1g per 100ml).
- swab with cotton using Nital 2% (etchant no. 74 according to Kundra, 2023) – electrolytic etching using a voltage of 8V.
- immersion in solution of 6.5ml HCl + 1.5ml HNO_3 + 1.8g CH_3COOH + 1.17ml H_2O.

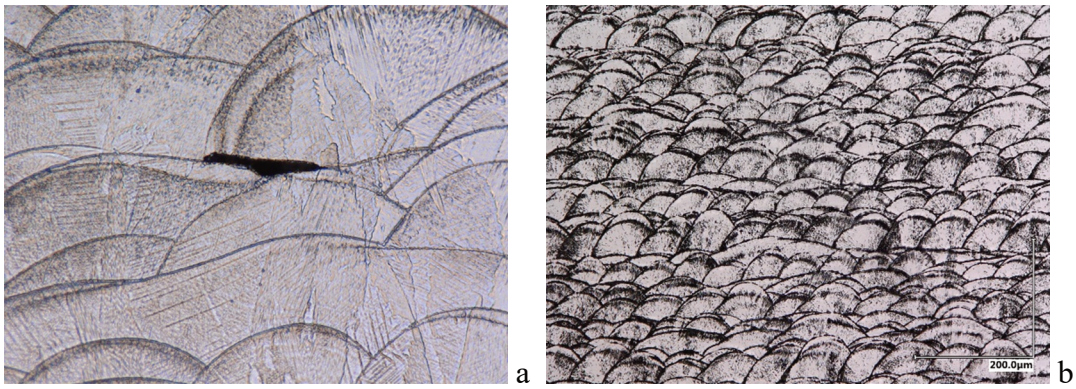

a b

Fig. 3. Effect of specimen etching with:
a) H_2O_2 solution in hydrochloric acid, (etchant no. 22 according to Kundra, 2023): 100ml HCl + 0.5ml H2O2 (30%)),
b) H_2O_2 solution in hydrochloric acid (ref. no. 22 according to Kundra, 2023): 100ml HCl + 0.5ml H_2O_2 (30 %)) – electrolytic etching at 4V,

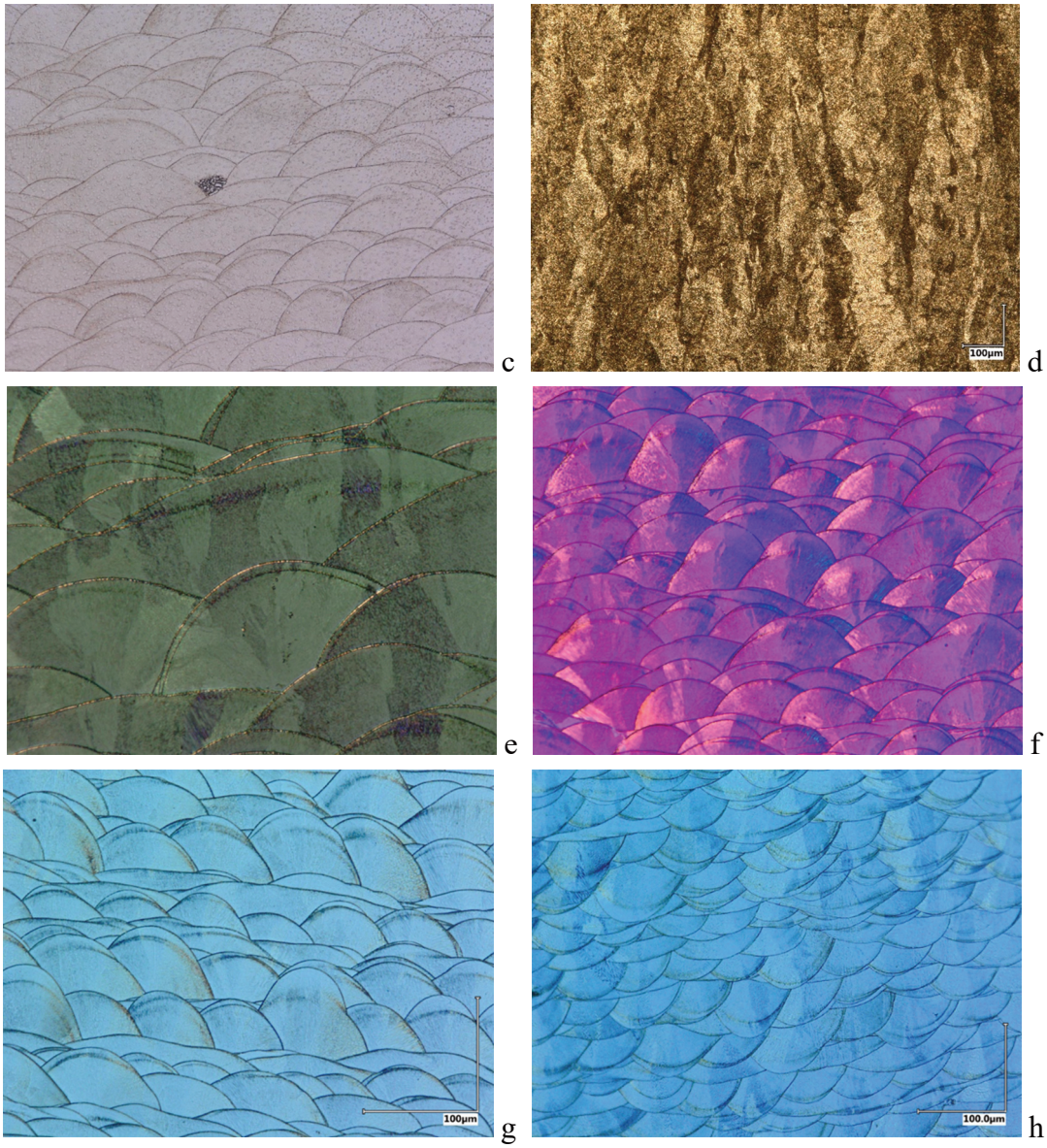

Fig. 3. Effect of specimen etching with:

c) 10% aqueous solution of oxalic acid – electrolytic etching at 6 V,
d) 38% aqueous solution of hydrochloric acid – 3h etching,
e) and f) 60 ml HNO_3 + 40 ml H_2O solution (ref. no. 219 according to Kundra, 2023) – electrolytic etching at 1 V – polarized light image,
g) Nital 2% (etchant no. 74 according to Kundra, 2023) – electrolytic etching at 8 V,
h) solution of 6.5 ml HCl + 1.5 ml HNO_3 + 1.8 g CH_3COOH + 1.17 ml H_2O.

The microstructural observations were performed on a Keyence VHS 6000 microscope. The revealed structure mainly represented boundaries corresponding to successive layers of the applied material. Some etchants revealed both layer and grain boundaries, but unfortunately the grain image was not clear.

etching method	observations	see Fig. 3
H_2O_2 solution in hydrochloric acid (etchant no. 22 according to Bhavar et al. (2017): 100 ml HCl + 0.5 ml H_2O_2 (30%)).	Promising results: the ability to distinguish grains based on the shade of their colors. Intense etching of melt boundaries and lack of etching of grain boundaries prevents their precise determination.	a
H_2O_2 solution in hydrochloric acid (ref. no. 22 according to Bhavar et al. (2017): 100 ml HCl + 0.5 ml H_2O_2 (30 %)) – electrolytic at 4 V.	Intensive etching of melt boundaries, grain boundaries invisible.	b
Kalling's etchant 1 and 2.	Etching effects were not obtained.	-
10% aqueous solution of oxalic acid – electrolytic etching at 6 V	Etching of melt boundaries, grain boundaries invisible.	c
38% aqueous solution of hydrochloric acid.	A 10-minute etching first extracted the boundaries of the melts. A 3-hour etching revealed grains, but there is difficulty in precisely defining their boundaries.	d
60 ml HNO_3 + 40 ml H_2O solution (ref. no. 219 according to Bhavar et al., 2017) – electrolytic etching at 1 V.	Promising results for observations with polarized light (the ability to distinguish grains based on the shade of their colors). Intense etching of melt boundaries and lack of etching of grain boundaries prevents their precise determination.	e, f
Berach's etchant III with the addition of sodium pyrosulfate (1 g per 100 ml).	No apparent etching effects were obtained.	-
Nital 2% (etchant no. 74 according to Kundra, 2023) – electrolytic etching at 8 V.	Etched melt boundaries in the first place, no etching of grain boundaries. Inability to distinguish between grains.	g
solution of 6.5 ml HCl + 1.5 ml HNO_3 + 1.8 g CH_3COOH + 1.17 ml H_2O.	Promising results for observations with polarized light (the ability to distinguish grains based on the shade of their colors). Intense etching of melt boundaries and lack of etching of grain boundaries prevents their precise determination.	h

The search for a suitable etchant to reveal grain boundaries did not yield a positive result. The possibility of using stress revealing anneal to eliminate the stresses suspected to be the effect of increased susceptibility to etching of melt boundaries is being considered. The optimal solution would be the EBSD method.

3.1.1. Material after annealing

In order to observe the microstructure, which is a combination of the effects associated with the application of the given five printing parameters sets as well as the heat treatment, five representatives for every printing set cubic specimens of $10\times10\times10$ mm^3 were prepared. The most optimal etchant among those tested in the first step was used, i.e. 60 ml HNO_3 + 40 ml H_2O solution (ref. no. 219 according to Bhavar et al., 2017), which yielded the promising microscope images shown in Figure 3e, f.

Electrolytic etching was carried at 0.75 V to 1.6 V, with optimal etching conditions obtained at about 1 V. Attempts were made to observe using polarized light. Also, in the case of the experimental cycle aimed at revealing the microstructure of the prints after heat treatment, the tests were performed on a Keyence VHS 6000 microscope.

It was found that annealing performed on a tested specimen largely reduced the ability of the selected etching method to reveal boundaries of melted material, but grain boundaries are still slightly visible. Their correct recognition is additionally hindered by the high density of the slip bands that appeared in the material after annealing. The traces of slip bands on the heat-treated specimens are arranged in a rhombic pattern with a dilation angle of about 120°, which corresponds to the phase transformation from a face-centered to a hexagonal system observed during diffraction studies (see Fig. 5 and Table 4 in paragraph 3.2).

The microstructure results for specimens after heat treatment sets no. 1–5 are shown in Fig. 3. The microscopy observations of each specimen were performed in two planes:

- in a plane parallel to the applied material layer (Z),
- in a plane perpendicular to the applied material layer (X).

The specimens were etched with different times to reveal the microstructure. Specimens etched in the plane of the applied material layer (Z) are characterized by grain regularity (small difference between the largest and smallest chord, e.g. Fig. 4a, g). On the other hand, the grains visible on the planes perpendicular to the applied material layer (X) have a columnar shape, which is related to the temperature gradient and the direction of crystallization (e.g. Fig. 4b, h).

In some of the etched metallographic specimens, slip bands appeared, arranged relative to each other in diamond shapes with an opening angle of 120°. This phenomenon is most pronounced in specimens with low porosity (no. 1, 3, 5). In specimens with the highest porosity (no. 2 and 4) this effect is much more difficult to see. It interferes with the optical identification of grain boundaries, thus preventing accurate statistical analysis of the microstructure. Despite this obstacle, the parameters of the manufacturing process can be seen to have a significant effect on the microstructure of the material – differences in grain size are discernible. Specimen no. 5, produced with the highest energy density (Fig. 4i, j), is characterized by significantly larger grain sizes than the other specimens (Fig. 4a–h). This phenomenon is probably related to the phase transformation, change in elementary cell dimensions and plastic deformation occurring during heat treatment.

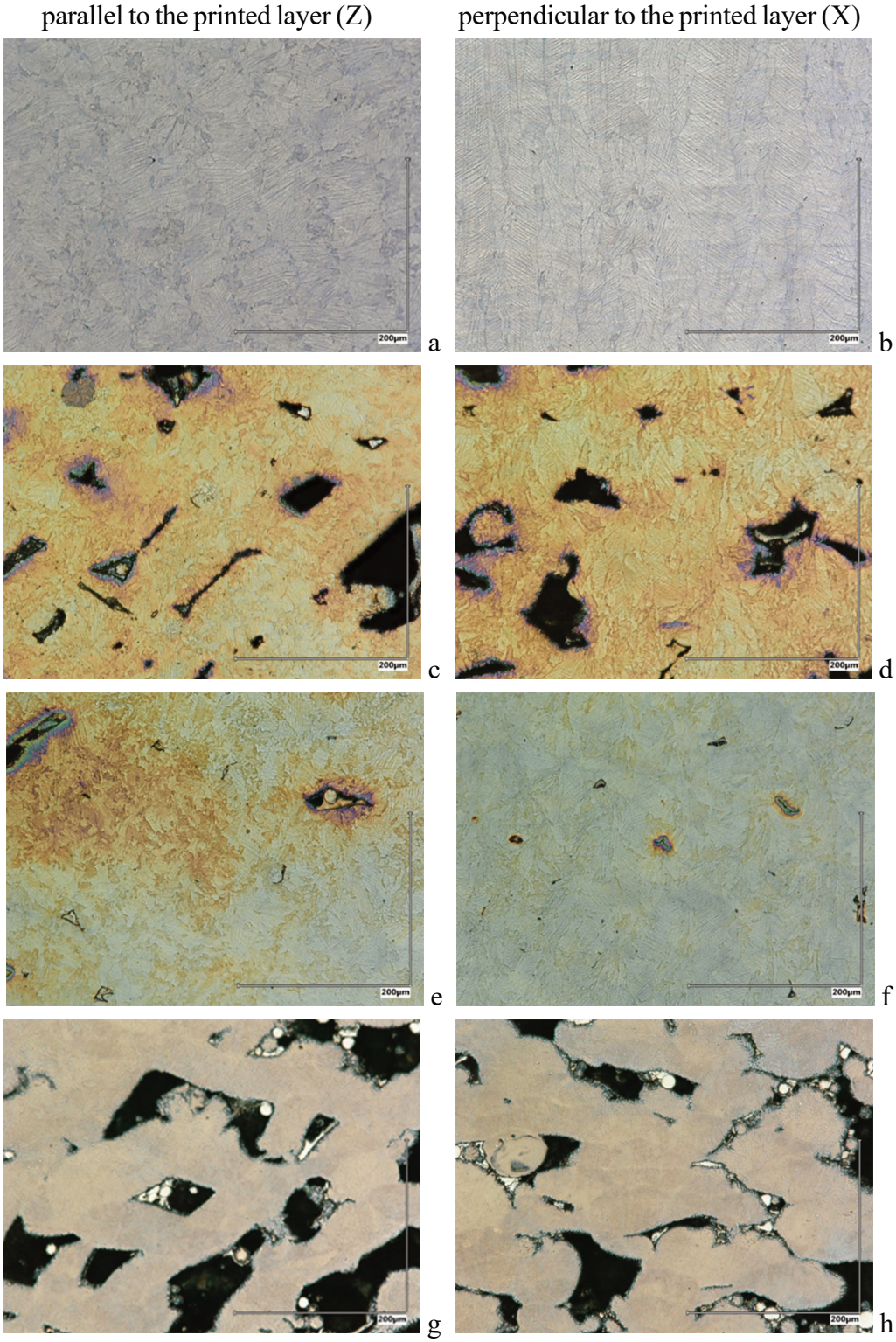

Fig. 4. Microstructure of specimen no. 1 (a, b), no. 2 (c, d), no. 3 (e, f), no. 4 (g, h).

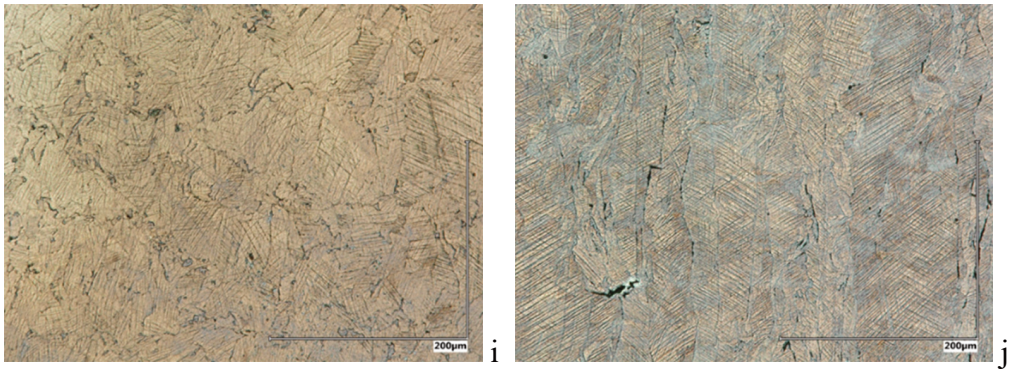

i j

Fig. 4. Microstructure of specimen no. 5 (i, j).

In general, the revealed structure represented grain boundaries. Grain surface of the heat-treated specimens shows slip bands caused by plastic deformation and phase transformation from the heat treatment process (no recrystallization of the material was observed). Traces of slip bands disrupt the microstructure image and make it difficult to identify grain boundaries.

3.2. Phase analyses

All diffraction experiments were carried out using an EMPYREAN diffractometer from MALVERN PANalytical.

Phase composition measurements were made for specimens in two states: before and after heat treatment. Phase analyses before heat treatment were carried out on specimens of cubic geometry with an edge length of 10 mm. During the experiment, $K_{\alpha 1}$ characteristic radiation from a copper X-ray tube was used, with the wavelength of $\lambda = 1.540598$ Å. X-ray polycapillary lenses with a length of 70 mm and a diameter of 7 mm were used in the path of the incident beam. In addition to the function of focusing X-rays, lenses ensure the formation of a quasi-parallel beam in two mutually perpendicular planes. This is particularly important when trying to realize measurements for rough surfaces. A 0.02 mm thick nickel filter was used to eliminate the K_{β} component of copper X-ray tube radiation. Radiation that diffracted on the planes of the crystal lattice was recorded by a semiconductor detector, which operated in scanning line detector mode.

A 7.5×2.5 mm^2 measuring spot was used to perform the measurements for the specimen before heat treatment. The heat treatment aimed to relax residual stresses. The detector setting options used a narrowed detection range of 8.85 keV to 12.88 keV. The minimum value of the Bragg angle was 5º and the maximum value was 152º. A 2θ angle step of about 0.1° was used and it allowed detection of the diffraction image in 1402 steps. The measurement duration for one step was about 20 minutes. Based on the measurements, the diffractogram presented in Fig. 5 was obtained.

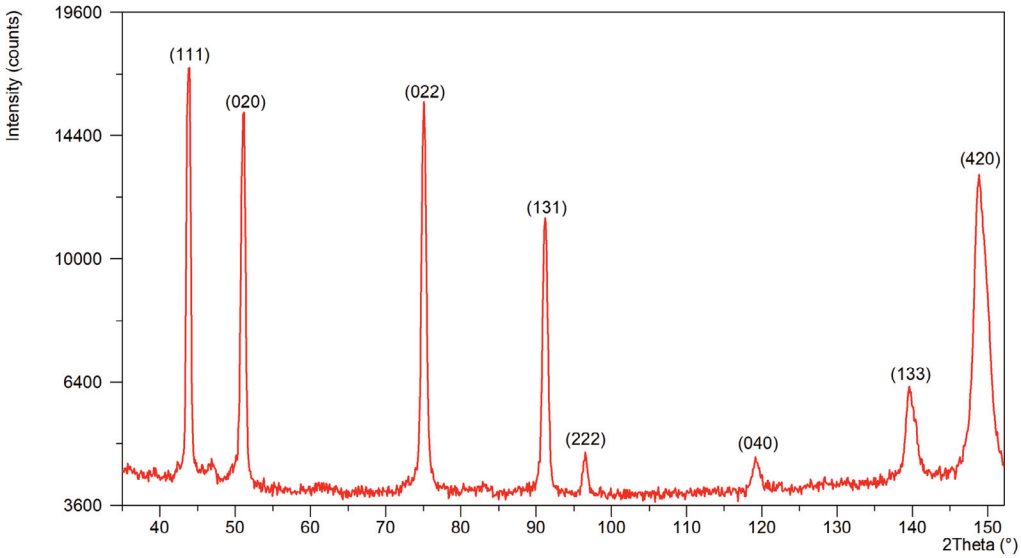

Fig. 5. X-ray diffractogram obtained for the specimen before heat treatment with the Braggs reflections indexed.

The indexing of diffraction reflections was carried out based on the results of Rietveld analysis, performed using HighScore4.7a software and based on ICCD PDF-4+ libraries version 2022 (Gates-Rector & Blanton, 2019). The Rietveld analysis results are presented in .

Table 3. Phase analysis results for the specimen before heat treatment.

phase	**ICDD card no.**	**structure space group**	**lattice parameters [Å]**	**%**
$W_{0.12}Co_{0.88}$	04-003-2728	cubic FCC Fm-3m 225	$a_0 = 3.586$	73.7
$Cr_{0.38}\ Co_{0.62}$	04-002-1030	hexagonal P63/mmc 194	$a_0 = b_0 = 2.53$ $c_0 = 4.08$	12.4
Co	04-006-8066	hexagonal P63/mmc 194	$a_0 = b_0 = 2.052$ $c_0 = 4.09$	11.4
$Mo\ Co_3$	04-004-3529	hexagonal P63/mmc 194	$a_0 = b_0 = 5.1245$ $c_0 = 4.1125$	2.5

The indexing was referred to the dominant phase component, that is, a phase composed of cobalt and tungsten in a face-centered cubic structure. The percentage of this phase was about 74%. The remaining phase components formed a hexagonal component.

The measurement of the phase composition for the heat-treated specimen was realized for a specimen dedicated to fatigue tests with a cylindrical shape. Copper

X-ray tube radiation was also used for this experiment, but the measurement spot size had to be changed to 10×1 mm^2 due to the specific geometry of the specimen. For this measurement, a larger range of radiation detection by the detector was used: ranging from 5.63keV to 12.88keV.

The Fig. 6 presents the full diffractogram for the heat-treated specimen. Rietveld analysis showed the existence of two main phase components in the specimen material (cf. Table 4): $Cr_{0.8}Co_{0.2}$ with a hexagonal close packed structure (44.5%) and Co_3O_4 with a cubic structure (32.3%). Fig. 6 shows the identification of the two main phase components of the specimen as well as the indexing of the most intense crystallographic reflections of each phase.

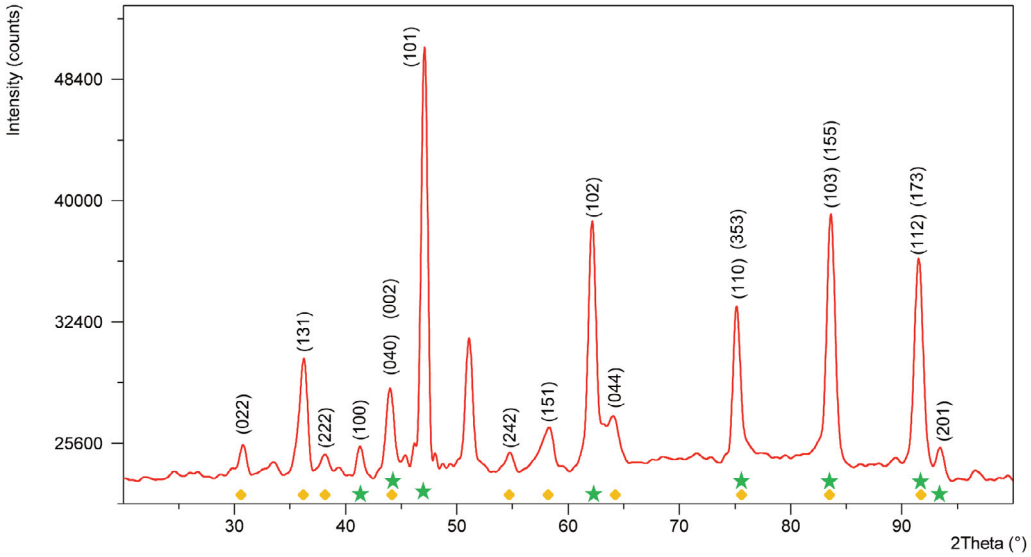

Fig. 6. X-ray diffractogram obtained for the specimen after heat treatment with the Braggs reflections indexed: the yellow square corresponds to reflections of the cubic Co_3O_4 phase and the green stars to reflections of the hexagonal $Cr_{0.8}Co_{0.2}$ phase.

Table 4. Phase analysis results for the specimen after heat treatment.

phase	**ICDD card no.**	**structure space group**	**lattice parameters [Å]**	**%**
$Cr_{0.8}Co_{0.2}$	01-071-7109	hexagonal P63/mmc 194	$a_0 = b_0 = 2.52$ $c_0 = 4.062$	44.5
$W_{0.04}Co_{0.96}$	04-003-2727	hexagonal P63/mmc 194	$a_0 = b_0 = 2.523$ $c_0 = 4.083$	16.4
$W_{0.12}Co_{0.88}$	04-003-2728	cubic FCC Fm-3m 225	$a_0 = 3.586$	6.8
Co_30_4	04-014-7747	cubic Fd-3m 227	$a_0 = 8.1773$	32.3

As a result of the phase analyses carried out for the as-built printed specimen as well as after the dedicated heat treatment, there was a change in the relative content of the cubic and hexagonal closed packed structures. After the heat treatment, recrystallization must have occurred, in which the hcp-structured (hexagonal closed packed) phase had a much higher final share. The share of the cubic phase in the specimen before heat treatment was 73.7%, whereas after heat treatment this value dropped to 39.1%. The total share of the hcp phase in the specimen without heat treatment was 26.3%, while after heat treatment this value increased to 60.9%. Notably, cobalt oxide (Co_4O_3) was detected on the surface of the heat-treated specimen. The identified structural change will certainly affect the properties and strength of the components produced in this way and subjected to such thermal treatment.

3.3. Stress measurements

During the research cycle, the first approach sought to capture the variation of stress values predicted by numerical models along the axis of each specimen. To this end, collimation of the X-ray beam through a 0.3 mm diameter monocapillary was used. Unfortunately, due to the high level of surface roughness, with such a relatively small-volume specimen in the diffraction experiment, the predicted variability of the residual stress level could not be captured, or such variability did not actually occur. Nevertheless, the averaged measurement using a monocapillary for 5 equally spaced points along the specimen axis was consistent with the measurement result for a much larger measurement beam, i.e. 1×10 mm^2. In subsequent experimental investigations, it was decided to perform measurements for a much larger measurement spot: 1×10 mm^2 for the circumferential stress direction with respect to the specimen geometry and 1×5 mm^2 for the axial stress direction. In the case of both types of measurements, those aimed at determining the value of the stresses in the circumferential direction and those in accordance with the direction determined by the sample axis, the dimension by 1 mm corresponded with the circumferential direction. The reduced measurement dimension along with the axis of the specimens in the case of axial stress measurement was related to the specific requirements of stress measurement and the associated increase in the size of the measurement spot, as the beam incident on the specimen was tilted in a given direction.

All measurements to obtain information on the level of residual stresses were carried out based on the standardized $\sin^2\psi$ method. During all stress measurements for both the specimens before and after heat treatment, a polycapillary, previously used in measuring the phase composition, was applied on the incident beam, and the detection of the diffracted radiation was carried out using a semiconductor detector operating in scanning line detector mode (the energy detection range of diffracted photons for these measurements was 8.85 keV to 12.88 keV).

During the measurement performed out for specimens prior to heat treatment, copper X-ray tube radiation and a nickel filter were used. The measurements were carried out in OMEGA mode for diffraction peaks becoming from planes with Miller indices hkl = 133. Each measurement was realized with a $\sin^2\psi$ step equal to 0.2. Each diffraction peak was detected in the angular range of 2θ equal to about 8° with a step of 0.13°. When analyzing the experimental results, the following material constants were assumed: $s_1 = -1.39$ 1/TPa and $\frac{1}{2}\, s_2 = 5.59$ 1/TPa.

The experiment yielded the stress values presented in Fig. 7 – Fig. 8.

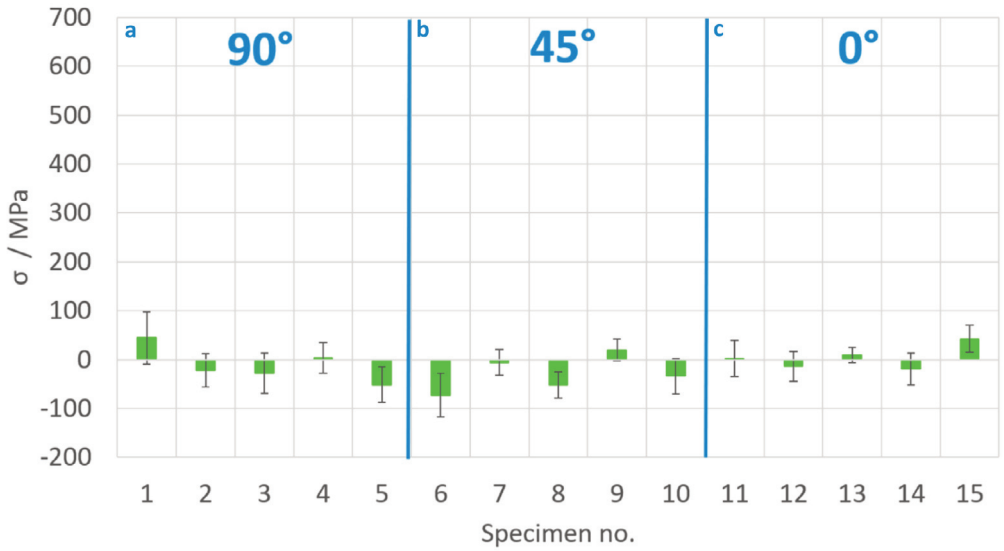

Fig. 7. Results of stress measurements in the circumferential direction before heat treatment: a) for specimens with printing direction along the specimen axis, b) for specimens printed at an angle of 45° with respect to their axis, c) for specimens printed in a direction perpendicular to their axis.

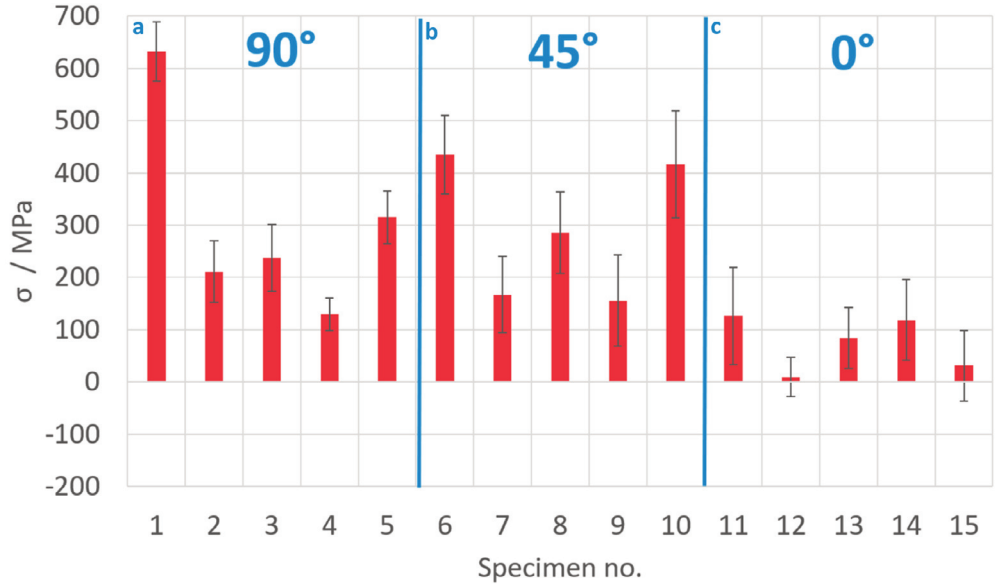

Fig. 8. Results of stress measurements in the axial direction before heat treatment: a) for specimens with printing direction along the specimen axis, b) for specimens printed at an angle of 45° with respect to their axis, c) for specimens printed in a direction perpendicular to their axis.

The values of circumferential stresses for the specimens directly after printing, for each of the printing directions, were close to zero. The average for all printing directions

was –12 MPa. The results of stress measurements for the axial direction were completely different. In the latter case, mainly for the 90° and 45° printing directions, significant tensile stresses were observed in the range from about 130 MPa to 630 MPa, on average: about 300 MPa (for the printing direction in line with the specimen axis) and from 155 MPa to 435 MPa, average: about 290 MPa (for the 45° direction). Specimens printed in the direction perpendicular to the axis were characterized by stresses up to about 100 MPa, average: about 75 MPa.

Stress measurements for the heat-treated specimens were carried out using X-ray tube radiation with a manganese anode. The wavelength of the radiation was $K_{\alpha 1}$ = 2.10187 Å. The detection was carried to diffraction reflection for which the Bragg's angle was about 147.2° degrees. The other measurement parameters remained the same as for the specimens before heat treatment. The results of the stress measurements for the heat-treated specimens are shown in Fig. 9 – Fig. 10.

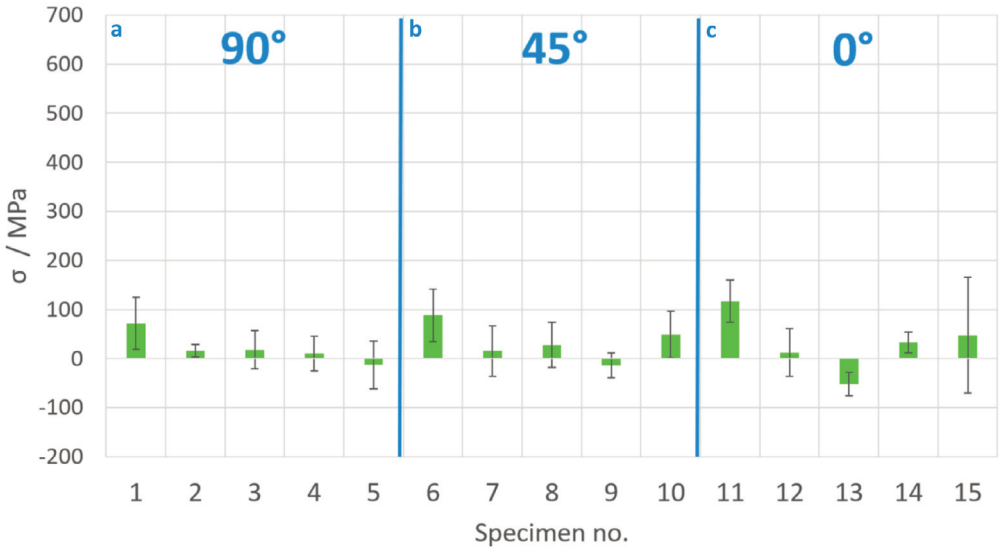

Fig. 9. Results of stress measurements in the circumferential direction after heat treatment: a) for specimens with printing direction along the specimen axis, b) for specimens printed at an angle of 45° with respect to their axis, c) for specimens printed in a direction perpendicular to their axis.

The stresses in the circumferential direction after the dedicated treatment did not change significantly, their values did not exceed 120 MPa while their average value was less than 30 MPa. The stresses in the axial direction changed significantly, especially for the directions of the print in line with the specimen axis (90°) and at 45° relative to the specimen axis. For printing in line with the specimen axis, the stresses took on a compressive character with absolute values below 100 MPa and average about –50 MPa. For a specimen printed at an angle of 45° with respect to the specimen axis, there was no change in the nature of the stresses but their value decreased: the highest stress value was measured for specimen no. 8, at about 150 MPa, with an average of 80 MPa for this type of specimen. Stress values for specimens whose printing direction was perpendicular to their axis did not change after heat treatment and averaged about 105 MPa.

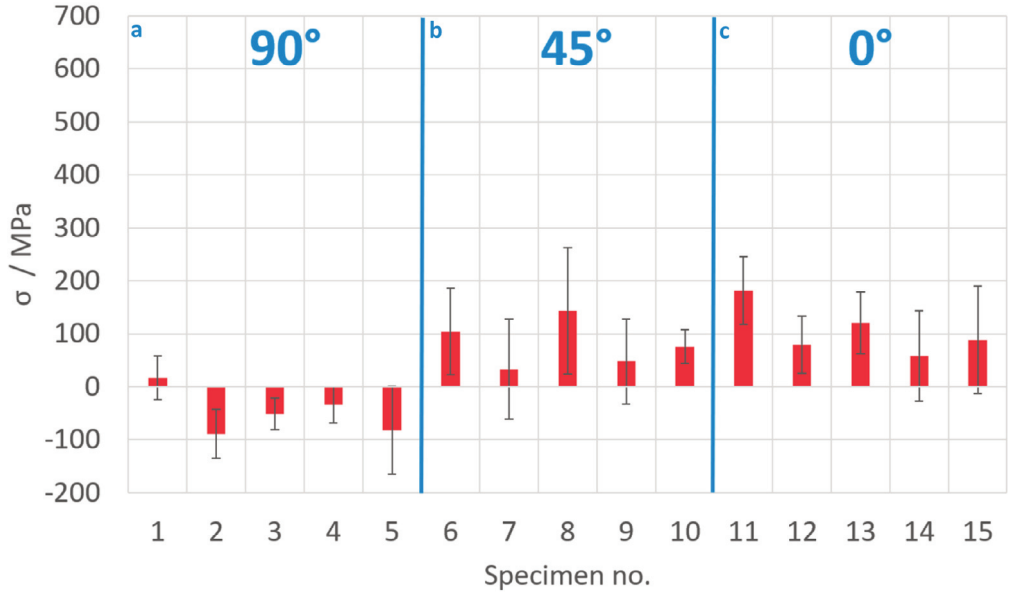

Fig. 10. Results of stress measurements in the axial direction after heat treatment: a) for specimens with printing direction along the specimen axis, b) for specimens printed at an angle of 45° with respect to their axis, c) for specimens printed in a direction perpendicular to their axis.

4. CONCLUSIONS

Our study's findings support several conclusions regarding the relationship between printing strategies, porosity, and residual stresses in printed specimens.

Firstly, specimens exhibiting the highest porosity, specifically those printed using strategies 2 and 4, displayed the lowest residual stresses. This correlation suggests that the presence of pores within the material facilitates stress relaxation. The pronounced porosity observed in specimens from strategies 2 and 4 can be attributed to the lower energy densities applied (30.2 J/mm³ and 27.8 J/mm³, respectively), and possibly to a thicker single layer, especially noted in the case of strategy 2. However, merely reducing the thickness of a single layer did not significantly lower the porosity of the prints, as demonstrated by the specimens from strategy 4.

Secondly, a surprising outcome was noted for specimens 1 and 5, where the printing direction was aligned with the specimen's axis, and the energy density values were relatively similar. Specimen 1, printed with strategy 1, exhibited considerably higher compressive stresses (over 600 MPa), whereas specimen 5, printed using strategy 5, showed stresses that were about half as much (around 300 MPa). When printed at a 45° angle relative to the specimen axis or perpendicular to it, the stress differences between specimens from strategies 1 and 5 were marginal. These findings indicate that the choice of printing direction relative to the part's geometry, among other parameters, plays a crucial role in determining the final properties of the printed parts.

Lastly, regarding strategy 3, although a relatively high power setting was used, the scanning speed was significantly increased compared to strategy 5, and both the single layer thickness and hatch spacing were slightly enlarged. This parameter configuration

yielded average values of tensile circumferential stresses, underscoring the complex interplay between printing parameters and the mechanical stresses developed within he printed parts.

References

Barucca, G., Santecchia, E., Majni, G., Girardin, E., Bassoli, E., Denti, L., Gatto, A., Iuliano, L., Moskalewicz, T., & Mengucci, P. (2015). Structural characterization of biomedical Co–Cr–Mo components produced by direct metal laser sintering. *Materials Science and Engineering: C, 48*, 263–269. https://doi.org/10.1016/j.msec.2014.12.009

Behjat, A., Lannunziata, E., Gadalińska, E., Iuliano, L., & Saboori, A. (2023). Improving the surface quality and mechanical properties of additively manufactured AISI 316L stainless steel by different surface post-treatment. *Procedia CIRP, 118*, 771–776. https://doi.org/10.1016/j.procir.2023.06.132

Bhavar, V., Kattire, P., Thakare, S., Patil, S., & Singh, R. K. P. (2017). A review on functionally gradient materials (FGMs) and their applications. *IOP Conference Series: Materials Science and Engineering, 229*(1), 012021. https://doi.org/10.1088/1757-899X/229/1/012021

Gates-Rector, S., & Blanton, T. (2019). The Powder Diffraction File: a quality materials characterization database. *Powder Diffraction, 34*(4), 352–360. https://doi.org/10.1017/S0885715619000812

Gaytan, S. M., Murr, L. E., Martinez, E., Martinez, J. L., Machado, B. I., Ramirez, D. A., Medina, F., Collins, S., & Wicker, R. B. (2010). Comparison of microstructures and mechanical properties for solid and mesh cobalt-base alloy prototypes fabricated by electron beam melting. *Metallurgical and Materials Transactions A, 41*(12), 3216–3227. https://doi.org/10.1007/s11661-010-0388-y

Gong, H., Rafi, K., Gu, H., Starr, T., & Stucker, B. (2014). Analysis of defect generation in Ti–6Al–4V parts made using powder bed fusion additive manufacturing processes.*Additive Manufacturing, 1–4*, 87–98. https://doi.org/10.1016/j.addma.2014.08.002

Kajima, Y., Takaichi, A., Nakamoto, T., Kimura, T., Yogo, Y., Ashida, M., Doi, H., Nomura, N., Takahashi, H., Hanawa, T., & Wakabayashi, N. (2016). Fatigue strength of Co–Cr–Mo alloy clasps prepared by selective laser melting. *Journal of the Mechanical Behavior of Biomedical Materials, 59*, 446–458. https://doi.org/10.1016/j.jmbbm.2016.02.032

Kundra, Y. (2023). ASTM E407 Standard Practice for Microetching Metals and Alloys Laboratories, ASTM E407 Standard Practice for Microetching Metals and Alloys Testing Services in California, USA. Infinita Lab. Retrieved April 6, 2023, from https://infinitalab.com/astm/astm-e407-standard-practice-for-microetching-metals-and-alloys/

Lee, S.-H., Takahashi, E., Nomura, N., & Chiba, A. (2005). Effect of heat treatment on microstructure and mechanical properties of Ni- and C-free Co–Cr–Mo alloys for

medical applications. *Materials Transactions, 46*(8), 1790–1793. https://doi.org/10.2320/matertrans.46.1790

Lu, Y., Wu, S., Gan, Y., Li, J., Zhao, C., Zhuo, D., & Lin, J. (2015). Investigation on the microstructure, mechanical property and corrosion behavior of the selective laser melted CoCrW alloy for dental application. *Materials Science and Engineering: C, 49*, 517–525. https://doi.org/10.1016/j.msec.2015.01.023

Lu, Y., Wu, S., Gan, Y., Zhang, S., Guo, S., Lin, J., & Lin, J. (2016). Microstructure, mechanical property and metal release of As-SLM CoCrW alloy under different solution treatment conditions. *Journal of the Mechanical Behavior of Biomedical Materials, 55*, 179–190. https://doi.org/10.1016/j.jmbbm.2015.10.019

Mantrala, K. M., Das, M., Balla, V. K., Rao, C. S., & Rao, V. V. S. K. (2014). Laser-deposited CoCrMo alloy: Microstructure, wear, and electrochemical properties. *Journal of Materials Research, 29*(17), 2021–2027. https://doi.org/10.1557/jmr.2014.163

Mengucci, P., Barucca, G., Gatto, A., Bassoli, E., Denti, L., Fiori, F., Girardin, E., Bastianoni, P., Rutkowski, B., & Czyrska-Filemonowicz, A. (2016). Effects of thermal treatments on microstructure and mechanical properties of a Co–Cr–Mo–W biomedical alloy produced by laser sintering. *Journal of the Mechanical Behavior of Biomedical Materials, 60*, 106–117. https://doi.org/10.1016/j.jmbbm.2015.12.045

Monroy, K., Delgado, J., & Ciurana, J. (2013). Study of the Pore Formation on CoCrMo Alloys by Selective Laser Melting Manufacturing Process. *Procedia Engineering, 63*, 361–369. https://doi.org/10.1016/j.proeng.2013.08.227

Pathak, S., Böhm, M., Kaufman, J., Kopeček, J., Zulić, S., Stránský, O., Shukla, A., Brajer, J., Beránek, L., Radhakrisnan, J., Rostohar, D., & Mocek, T. (2023). Surface integrity of SLM manufactured meso-size gears in laser shock peening without coating. *Journal of Manufacturing Processes, 85*, 764–773. https://doi.org/10.1016/j.jmapro.2022.12.011

Qian, B., Saeidi, K., Kvetková, L., Lofaj, F., Xiao, C., & Shen, Z. (2015). Defects-tolerant Co-Cr-Mo dental alloys prepared by selective laser melting. *Dental Materials, 31*(12), 1435–1444. https://doi.org/10.1016/j.dental.2015.09.003

Sun, S.-H., Koizumi, Y., Kurosu, S., Li, Y.-P., Matsumoto, H., & Chiba, A. (2014). Build direction dependence of microstructure and high-temperature tensile property of Co–Cr–Mo alloy fabricated by electron beam melting. *Acta Materialia, 64*, 154–168. https://doi.org/10.1016/j.actamat.2013.10.017

Takashima, T., Koizumi, Y., Li, Y., Yamanaka, K., Saito, T., & Chiba, A. (2016). Effect of Building Position on Phase Distribution in Co-Cr-Mo Alloy Additive Manufactured by Electron-Beam Melting. *Materials Transactions, 57*(12), 2041–2047. https://doi.org/10.2320/matertrans.Y-M2016826

Wang, W. J., Yung, K. C., Choy, H. S., Xiao, T. Y., & Cai, Z. X. (2018). Effects of laser polishing on surface microstructure and corrosion resistance of additive manufactured CoCr alloys. *Applied Surface Science, 443*, 167–175. https://doi.org/10.1016/j.apsusc.2018.02.246

Wei, D., Koizumi, Y., Chiba, A., Ueki, K., Ueda, K., Narushima, T., Tsutsumi, Y., & Hanawa, T. (2018). Heterogeneous microstructures and corrosion resistance of biomedical Co-Cr-Mo alloy fabricated by electron beam melting (EBM). *Additive Manufacturing, 24*, 103–114. https://doi.org/10.1016/j.addma.2018.09.006

Wei, D., Koizumi, Y., Takashima, T., Nagasako, M., & Chiba, A. (2018). Fatigue improvement of electron beam melting-fabricated biomedical Co–Cr–Mo alloy by accessible heat treatment. *Materials Research Letters, 6*(1), 93–99. https://doi.org/10.1080/21663831.2017.1396506

Wei, W., Zhou, Y., Liu, W., Li, N., Yan, J., & Li, H. (2018). Microstructural Characterization, Mechanical Properties, and Corrosion Resistance of Dental Co-Cr-Mo-W Alloys Manufactured by Selective Laser Melting. *J. of Materalsi Engineering and Performance, 27*(10), 5312–5320. https://doi.org/10.1007/s11665-018-3520-6

Xin, X., Chen, J., Xiang, N., & Wei, B. (2013). Surface properties and corrosion behavior of Co–Cr alloy fabricated with selective laser melting technique. *Cell Biochemistry and Biophysics, 67*(3), 983–990. https://doi.org/10.1007/s12013-013-9593-9

Zhou, X., Wang, D., Liu, X., Zhang, D., Qu, S., Ma, J., London, G., Shen, Z., & Liu, W. (2015). 3D-imaging of selective laser melting defects in a Co–Cr–Mo alloy by synchrotron radiation micro-CT. *Acta Materialia, 98*, 1–16. https://doi.org/10.1016/j.actamat.2015.07.014